Biofabrication

International Society for Biofabrication

PAPER

3D printing of sacrificial thioester elastomers using digital light processing for templating 3D organoid structures in soft biomatrices

To cite this article: Benjamin J Carberry *et al* 2021 *Biofabrication* **13** 044104

View the article online for updates and enhancements.

You may also like

- Engineering co-emergence in organoid models
Ivana Vasic and Todd C McDevitt
- Use of inkjet-printed single cells to quantify intratumoral heterogeneity
Woong Hee Yoon, Hwa-Rim Lee, SungEun Kim et al.
- Next generation human brain models: engineered flat brain organoids featuring gyrification
Theresa S P Rothenbücher, Hakan Gürbüz, Marta P Pereira et al.

BREATH® BIOPSY

Breath Biopsy® OMNI

The most advanced, complete solution for global breath biomarker analysis

SEE WHAT OMNI CAN DO FOR YOU

Expert Study Design & Management

Robust Breath Collection

Reliable Sample Processing & Analysis

In-depth Data Analysis

Specialist Data Interpretation

This content was downloaded from IP address 128.138.64.244 on 01/12/2021 at 21:25

Biofabrication

PAPER

3D printing of sacrificial thioester elastomers using digital light processing for templating 3D organoid structures in soft biomatrices

RECEIVED
13 April 2021

REVISED
16 July 2021

ACCEPTED FOR PUBLICATION
11 August 2021

PUBLISHED
2 September 2021

Benjamin J Carberry[1,2], John E Hergert[3], F Max Yavitt[1,2], Juan J Hernandez[1,2], Kelly F Speckl[1], Christopher N Bowman[1,2,3], Robert R McLeod[3,4] and Kristi S Anseth[1,2]

[1] Department of Chemical and Biological Engineering, University of Colorado Boulder, Boulder, CO 80303, United States of America
[2] The BioFrontiers Institute, University of Colorado Boulder, Boulder, CO 80303, United States of America
[3] Materials Science and Engineering, University of Colorado, Boulder, CO 80309, United States of America
[4] Department of Electrical, Computer and Energy Engineering, University of Colorado, Boulder, CO 80309, United States of America

E-mail: Kristi.Anseth@colorado.edu

Keywords: biofabrication, intestinal organoids, 3D printing, covalent adaptable networks, thioester exchange, stimuli-induced degradation

Supplementary material for this article is available online

Abstract

Biofabrication allows for the templating of structural features in materials on cellularly-relevant size scales, enabling the generation of tissue-like structures with controlled form and function. This is particularly relevant for growing organoids, where the application of biochemical and biomechanical stimuli can be used to guide the assembly and differentiation of stem cells and form architectures similar to the parent tissue or organ. Recently, ablative laser-scanning techniques was used to create 3D overhang features in collagen hydrogels at size scales of 10–100 μm and supported the crypt-villus architecture in intestinal organoids. As a complementary method, providing advantages for high-throughput patterning, we printed thioester functionalized poly(ethylene glycol) (PEG) elastomers using digital light processing (DLP) and created sacrificial, 3D shapes that could be molded into soft ($G' < 1000$ Pa) hydrogel substrates. Specifically, three-arm 1.3 kDa PEG thiol and three-arm 1.6 kDa PEG norbornene, containing internal thioester groups, were photopolymerized to yield degradable elastomers. When incubated in a solution of 300 mM 2-mercaptoethanol (pH 9.0), 1 mm thick 10 mm diameter elastomer discs degraded in <2 h. Using DLP, arrays of features with critical dimensions of 37 ± 4 μm, resolutions of 22 ± 5 μm, and overhang structures as small as 50 μm, were printed on the order of minutes. These sacrificial thioester molds with physiologically relevant features were cast-molded into Matrigel and subsequently degraded to create patterned void spaces with high fidelity. Intestinal stem cells (ISCs) cultured on the patterned Matrigel matrices formed confluent monolayers that conformed to the underlying pattern. DLP printed sacrificial thioester elastomer constructs provide a robust and rapid method to fabricate arrays of 3D organoid-sized features in soft tissue culture substrates and should enable investigations into the effect of epithelial geometry and spacing on the growth and differentiation of ISCs.

1. Introduction

Organoids can develop from single stem cells when subjected to biochemical and biophysical cues that activate proper signaling pathways, which drive self-assembly into multicellular tissue constructs that are capable of recapitulating key aspects of the parent organ or tissue [1, 2]. Interest in the culture of organoids has grown in recent years, with applications in drug screening, tissue for transplantation, and for disease modeling [1]. The cellular and functional sophistication of organoids relates to the ability of the stem cells to self-organize, differentiate into relevant cell types, and organize into structures

© 2021 IOP Publishing Ltd

that are similar to the parent organ from which they were derived. For example, intestinal stem cell (ISC) colonies grow and form crypt-like protrusions from the central lumen *in vitro*, generating architectures reminiscent of the crypt-villus axis *in vivo* [2, 3]. To date, most organoids, including intestinal organoids, are grown in Matrigel, which typically leads to structures that are stochastically variant in shape and size [4, 5]. To address some of these heterogeneities, recent work has developed synthetic biomaterial matrices for intestinal organoid culture, where the biomaterial chemistry and time-varying properties (e.g. elastic modulus) are used to control the size, structure, and periodicity of the crypt-villus structures [6, 7]. We and others have posited that organoid function will depend on form, so efforts have focused on introducing physiologically relevant architectures, templates, or molds to precisely control the size and shape of lab-grown intestinal organoids.

While recent advances in fabrication techniques have allowed intimate control over the structure, architecture, and properties of many classes of biomaterials, some of the methods are limited to features sizes $\geqslant$100 μm [8], and others are not compatible with printing in many biological matrices (e.g. collagen, Matrigel) [9]. Here, we were interested in printing features sizes (<100 μm) that could be transferred to Matrigel ($G < 1000$ Pa), resulting in templated culture wells for intestinal organoids. To date, soft lithographic techniques, such as poly(dimethyl siloxane) (PDMS) stamps, have been used to transfer pseudo-3D architectures to soft materials, such as collagen. Typically, the positive PDMS features are pressed into collagen solutions during gelation to form a cast mold of the original pattern. Removal of the PDMS stamp leaves the freestanding culture substrate with patterned negatives of the PDMS features. Wang *et al* used PDMS stamps to generate arrays of crypt-villi structures in stiff collagen hydrogels, which were then used to culture ISCs and led to spatially restricted lineages reminiscent of the *in vivo* intestinal epithelium [10]. While this method provides many advantages, the PDMS stamp must be removed, so patterns with overhang features embedded within the matrix cannot be fabricated.

To build upon and complement the PDMS stamping method, researchers have also used extrusion-based, sacrificial molds [11]. These molds have been embedded within biologically-relevant biomaterial scaffolds and subsequently dissolved in place to generate complex, three-dimensional tissue scaffolds [12]. In one example, Miller *et al* [13] printed a carbohydrate material into rigid fibers that could be embedded and rapidly dissolved in aqueous solutions to create networks of channels to generate a wide range of cell-laden materials. For example, hepatocytes seeded at high density in these thick, perfusable materials showed improved cell survival and enzymatic function [13]. Expanding on this approach, Koleski *et al* integrated temperature-sensitive hydrogel inks (e.g. gelatin, pluronics) into a multi-material printing platform to print fugitive vasculature structures [14, 15]. While the shear thinning behavior of temperature sensitive inks enabled direct printing of sacrificial channels [8], the low modulus of the inks necessitated printing within a supportive substrate, preventing the formation of free standing structures. Thus, although these techniques allow for the fabrication of overhanging features and features embedded within bioscaffolds, the methods are limited by the size and resolution that can be achieved ($\geqslant$100 μm) [8]. Because of this, these approaches less relevant for directing intestinal organoid growth and differentiation.

Alternatively, photochemical fabrication techniques have been widely used to pattern materials at sub-cellular resolution [16–19]. For example, Nikolaev *et al* used photoablation of collagen/Matrigel composites to generate a 150 μm diameter tube that was further processed to integrate 50 μm wide and 170 μm long crypt projections [17]. When seeded with ISCs, an epithelial cell monolayer grew and conformed to the photoablated pattern to yield the patterned crypt-villus architecture [17]. While photoablation offers high-resolution, spatial control over the patterned features, the process occurs voxel by voxel, rendering this strategy less amenable for generating large arrays of features for high throughput testing. Thus, we were motivated to apply digital light projection (DLP) to accelerate photopatterning speeds and create arrays of uniform features. DLP uses a spatial light modulator (SLM) array to print small feature sizes layer by layer rather than voxel by voxel [20]; however, photopolymer materials used in DLP can also serve as sacrificial, degradable molds [21, 22]. In one example, Thomas *et al* printed hyaluronic acid methacrylate based features and then embedded the mold in gelatin methacrylate before using hyaluronidase to erode the hyaluronic acid, yielding 300 μm diameter perfusable vasculature structures [22]. However, the degradation time of enzyme erodible constructs can vary from minutes to days depending on the hydrogel stiffness (i.e. crosslinking density), so there is a tradeoff when higher strength to weight ratios are needed in the mold to pattern freestanding or overhanging structures [23, 24]. In this contribution, we exploit recent advances in thioester exchange chemistry, which is compatible with photopolymerization reactions [25–27], and sought to design bioink formulations that would yield structurally robust elastomeric molds, but allow for rapid and gentle network degradation [28, 29].

Results herein report on the development of a degradable thioester-based elastomer resin for 3D printing and use DLP to print sacrificial, elastomer molds with critical dimensions of 37 $\pm$ 4 μm and *XY* resolutions of 22 $\pm$ 5 μm. Three-dimensional, negative mold structures were printed and then

cast into soft biomaterials matrices, Matrigel and poly(ethylene glycol) PEG hydrogels, that are suitable for organoid growth. A reversible exchange reaction between 2-mercaptoethanol in solution with thioester crosslinks in the printed structures lead to rapid degradation at pH 9.0 T 25 °C, effectively transferring these complex patterns to the hydrogel material. This pattern transfer was characterized as a function of feature size, resolution and depth for soft ($G < 1000$ Pa) PEG and Matrigel hydrogels. Overhanging structures 150 μm in diameter were either printed close together (<50 μm) or with perpendicular overhanging cylindrical features ($D > 50$ μm). Features were produced in arrays 50 at a time on the timescale of ∼20 min. The printed structures transferred to Matrigel with high fidelity to form shapes relevant to the crypt-villus structures found in intestinal epithelium and intestinal organoids. Finally, we show Matrigel hydrogels patterned with this technique support the culture of ISC monolayers, which formed confluent layers and conformed to the patterned structures.

2. Materials and methods

2.1. Synthesis of three-arm PEG thiol (1300 Da)

The PEG thiol synthesized has been previously described [30]. In brief, 14.06 ml of glycerol ethoxylate (1000 Da, Sigma–Aldrich) and 8.4 ml of 3-mercaptopropionic acid were combined in a 1000 ml round bottomed flask equipped with a stir bar, deanstark trap, condenser, and oil bath. 300 ml of toluene were added through the condenser; then the mixture was heated to reflux for 5 min; three drops of sulfuric were added; and the vessel was stirred at reflux overnight. Next, toluene was removed in vacuo, and the mixture was redissolved in dichloromethane and purified with three washes of a saturated $NaHCO_3$ solution and one wash with brine. The remaining clear organic layer was then collected, dried over Na_2SO_4, and concentrated in vacuo to produce a clear viscous liquid. (>95% functionalized) 1H NMR (400 MHz, CDCl3) δ 4.32–4.19 (m, 6H), 3.86–3.42 (m, 85H), 2.83–2.72 (m, 6H), 2.72–2.62 (m, 6H), 1.72–1.62 (t, 3H)

2.2. Synthesis of three-arm PEG thioester norbornene

(1600 Da) 10.0 g of three-arm PEG thiol was combined with 13.65 g 1-ethyl-3-(3-dimethylaminopropyl)carbodiimide in a flame dried 1000 ml round-bottomed flask equipped with a stir bar. 400 ml of anhydrous dichloromethane were added via cannula followed by 5.8 ml of 5-norbornene-2-carboxylic acid (mixture of endo and exo, Alfa Aesar). After stirring under argon for 15 min, 17 ml of diisopropylethylamine were added to the vessel. After 15 min of argon, the apparatus was fixed with an argon balloon and allowed to stir overnight. The reaction mixture was diluted to a volume of 800 ml with fresh dichloromethane, then washed gently and quickly with seven washes of 300 ml 0.1 N hydrochloric acid. The organic layer was then washed three times with a saturated $NaHCO_3$ solution, once with brine, dried over Na_2SO_4, and then concentrated in vacuo to produce a clear, slightly yellow viscous liquid. (85% functionalized) ^{1}H NMR (400 MHz, $CDCl_3$) δ 6.52–5.78 (m, 6H), 4.32–4.19 (m, 6H), 3.86–3.42 (m, 85H) (figure S1 (available online at stacks.iop.org/BF/13/044104/mmedia)).

2.3. Elastomer formation

Lithium phenyl-2,4,6-trimethylbenzoylphosphinate (LAP) was dissolved in deionized water at a concentration of 86.2 mg ml^{-1}, and combined with thiol and thioester norbornene macromers in a molar ratio of 1 thiol:1 norbornene:0.01 LAP, resulting in a 97 wt% polymer solution that readily polymerized when exposed to 10 mW cm^{-2} 365 nm light for 15 min.

2.4. Mechanical measurements

Elastomer stress strain behavior quantified with a dynamic mechanical analyzer (DMA) (RSA-G2, TA Instruments). Specifically, 250 μm thick non-swollen elastomer samples were elongated at 0.1 mm s^{-1} crosshead speed to generate stress strain curves until failure. The Young's modulus (E) was calculated from the slope of the linear segment of the stress–strain curve between 5% and 10% strain. Values are presented as the average ±SD. To quantify glass transition behavior, Young's modulus and tan(delta) measurements were measured in tension at a frequency of 1 Hz, a strain of 0.03%, a preload force of 0.34 N, and a temperature ramp rate of 3° min^{-1}. Glass transition temperature was calculated as the peak of the tan(delta) curve.

2.5. Mass loss study

Thioester elastomer samples were polymerized in the shape of discs (diameter = 10 mm, thickness = 1 mm. Initial mass was measured and used to calculate the initial amount of polymer contained in each sample (m_{pi}). Elastomer samples were placed in separate 50 ml conical tubes and swollen in tris buffer (pH 9.0, 100 mM) for 1 h, then the solutions were replaced with 5 ml of either tris buffer or tris buffer with 300 mM 2-mercaptoethanol. The final pH of all solutions was adjusted to 9.0. The swollen mass (m_s) was calculated as the ratio of elastomer swollen mass after 1 h in pH 9.0 tris buffer relative to the dry mass measured after lyophilization. Next, all samples were trimmed to a diameter of 8 mm using a biopsy punch and placed in a bath of tris buffer on a DHR-3 rheometer (TA Instruments) and measured for their shear elastic modulus (G') (0.1% strain, 1 Hz). On the rheometer, an axial force was applied and adjusted between 0.5 and 2.0 N to prevent sample slippage.

Finally, elastomer samples were lyophilized for 48 h, removed from conical tubes, and placed on a zeroed balance to record dry polymer mass (m_p). All data were taken in triplicate.

2.6. Fourier transform infrared (FTIR) characterization

Real-time FTIR spectroscopy (Nicolet 6700, Madison, WI) was used to follow the functional group conversion and subsequent kinetic analysis. The FTIR was equipped with a KBr beam splitter and MCT/A detector. Monomer formulations were placed between polished NaCl plates, and a 405 nm LED (M405L3-C5, ThorLabs) at an intensity of 8 mW cm^{-2} was used to initiate polymerization of the thiol:ene network. Simultaneously, the disappearance of the peaks associated with the carbon–carbon double bond of the norbornene (3060 cm^{-1}) and the thiol (2555 cm^{-1}) were monitored as a function of exposure time. The area under the peaks (A) were measured before and during the light exposure yielding the conversion (X) as a function of time. X was calculated based on the disappearance of the peak associated with each reactive specie by:

$$X_{\text{species}} = 1 - \frac{A}{A_{\text{initial}}}. \quad (1)$$

A 60 s exposure was used for each sample, but samples were monitored up to 5 min on the FTIR to assess any dark polymerization.

2.7. 3D printing of thioester elastomers

A custom-built, DLP system designed for bottom-up 3D printing was used to produce all samples (figure 3(a)). A 405 nm LED (SOLIS-405C, Thorlabs) and a high resolution SLM (1920 × 1152 Analog SLM, Meadowlark Optics, measured extinction ratio of 99.3%) were used to project patterns of a precise light exposure (405 nm, 8 mW cm^{-2}, 30 s) onto the printing resin (i.e. thioester precursors). The exposure pattern was imaged onto the sample plane with demagnification, resulting in a pixel diameter at the sample plane of 4.6 μm. A glass slide was used as the build-stage. A slab of index matched PDMS filled with carbon black was used as a neutral density filter laminated to the build stage prevent back reflections [31]. A non-stick PDMS window was prepared using a Sylgard 184 Silicone Elastomer Kit (DOW CORNING) mixed at 10:1 weight ratio [32, 33]. Printed structures were washed overnight in 100% ethanol, then stored in ethanol until use.

2.8. Patterned elastomer staining and quantitative image analysis

Fluorescein (acid yellow 73, Sigma–Aldrich) was diluted in 100% ethanol to a final concentration of 2 mg ml^{-1} and warmed to dissolve the fluorescein. Thioester elastomer stamps were submerged in the fluorescein solution for 30 min, then dried in a vacuum oven for 30 min, and transferred to glass slides for imaging with laser scanning confocal microscopy (Zeiss LSM 710, Fluar 10× air, 0.5 NA, 1AU). Critical dimensions were measured for printed pillar structures 50 μm tall and 10–100 μm in diameter. Resolution was measured for printed pillar structures 100 μm diameter and 50 μm tall spaced 10–100 μm. A z-stack (2.25 μm step) of each structure was taken, then an image slice 10–20 μm below the top of the feature was selected for analysis. This was done to avoid any surface effects that may be introduced on the top layer of the print. The images were then quantitatively analyzed in MATLAB. Each image was first turned into a binary image using the graythresh() and imbinarize() functions. Diameter was quantified in the critical dimension tests using the 'EquivDiameter' field of the regionprops() function. The spacing between pillars for the resolution tests was then quantified by taking the complement of the binary image and calling the improfile() function to measure pillar separation at the narrowest point. All data reported consist of $n = 3$ stamps with three technical replicates averaged together from each stamp.

2.9. Scanning electron microscopy (SEM)

Printed thioester samples were removed from the ethanol wash solution and allowed to dry in ambient conditions for 24 h uncoated thioester elastomer samples with 3D printed overhang structures were visualized on a SEM (Hitachi SU3500) using the secondary electron emission mode at an accelerating voltage of 5 kV.

2.10. Hydrogel formation and pattern transfer

PEG hydrogels were formed by photo-crosslinking the norbornene functionalized 20 kDa eight-arm PEG macromer with a thiol functionalized two-arm 5 kDa PEG macromer. The two macromers were combined in a 1:1 stoichiometric ratio and diluted with 1× phosphate buffered saline (PBS) to a final formulation containing 2.0 wt% polymer, 1 mM LAP photoinitiator, and 1 mg ml^{-1} 2000 kDa FITC dextran to facilitate direct hydrogel imaging. When irradiated with 10 mW cm^{-2} of 365 nm light for 60 s, a hydrogel with a final shear elastic modulus (G') of 740 ± 50 Pa forms (figure S2).

Elastomer stamps, composed of a 100 μm thick base with printed features on the top, were trimmed with an 8 mm biopsy punch, submerged in 100% ethanol in a conical tube, then brought into a tissue culture hood to maintain sterility. After 10 min of swelling in ethanol, the ethanol was replaced with 1× PBS, and the elastomer stamps swelled for 1 h. Hydrogel prepolymer mixtures, either 2 wt% PEG or Matrigel (corning), were placed in an ice bath along with a 10 cm × 10 cm × 1 cm sterilized steel block. Elastomer stamp manipulation was conducted as previously described [34, 35]. Briefly, the elastomer stamps were placed on the chilled block

with the features facing up, and excess water was gently aspirated. Each elastomer stamp was then quickly washed with 2 × 20 μl of pre-gel mixture for 30 s each to remove excess water from the pattern surface. Then, 20 μl of pre-gel mixture were dispensed onto 12 mm coverslips functionalized with (3-mercaptopropyl)trimethoxysilane (Sigma–Aldrich) placed into six well culture plates. Stamps were placed face-down to submerge printed features in pre-gel mixture, then gelation was induced. The Matrigel samples were placed in an incubator for 15 min to induce gelation. PEG samples were irradiated through the coverslip with 10 mW cm^{-2} 365 nm light for 60 s to induce gelation. Next, each stamp-hydrogel complex was washed twice with 3 ml of a pre-warmed solution containing 100 mM tris, 300 mM 2-mercaptoethanol at pH 9.0 (2 h then 1 h, 37 °C). Finally, patterned samples were washed 3× with pre-warmed PBS and stored in the incubator until use.

2.11. Patterned hydrogel staining and image analysis

To visualize the patterned Matrigel hydrogels, samples were first transferred to a 24 well plate washed with 1 ml of pre-warmed pH 9.0 100 mM $NaHCO_3$ for 10 min, followed by 500 μl of 0.031 mg ml^{-1} fluorescein isothiocyanate (invitrogen) in the same bicarbonate buffer. After 1 h, patterned Matrigel samples were then washed three times with PBS and stored in an incubator until imaging with confocal microscopy (Zeiss LSM 710, Plan-Aprochromat 20× water, 1.0 NA, 1AU). Measurements of well diameter and spacing were done by taking *z*-stack of each structure, then identifying an image slice 10–20 μm above the bottom of the well. These images were then quantitatively analyzed in MATLAB. Each image was first turned into a binary image using the graythresh() and imbinarize() functions. For patterned PEG hydrogels, diameter was quantified in the critical dimension tests by taking the complement of the binary image and using the 'EquivDiameter' field of the regionprops() function. Space between pillars was then quantified by calling the improfile() function to measure pillar separation at the narrowest point. For patterned Matrigel hydrogels, the improfile() function was used to measure both pillar separation and pillar diameter. All data reported consist of $n = 3$ stamps with three technical replicates averaged together from each stamp (figure S3).

2.12. Crypt isolation and organoid culture

Murine small intestinal crypts were extracted from Lgr5-eGFP-IRES-CreERT2 mice as previously described [6]. The crypts were cultured as organoids by first embedding them in reduced growth factor Matrigel (corning). The intestinal organoid cultures were maintained using Advanced DMEM-F12 (invitrogen), containing N2 and B27 supplements (Thermo Fischer Scientific), glutamax (gibco), HEPES, penicillin–streptomycin, and supplemented with epidermal growth factor (50 ng ml^{-1}, R&D Systems), Noggin (100 ng ml^{-1}, from collaborator), R-spondin conditioned media (5%), CHIR99021 (3uM, Selleckchem) and valproic acid (1 mM, Sigma–Aldrich). The medium was changed every 2 d, and organoids were passaged every 4 d.

2.13. Seeding of ISCs onto 2D gels

Intestinal organoids were released from Matrigel using cold media followed by mechanical stimulation from a pipette tip. The organoids were then enzymatically dissociated into single ISCs (that are Lgr5+ and express GFP) by incubation at 37 °C for 8 min in 1 ml TrypLE (Life Technologies), supplemented with DNAseI (∼10 mg, Sigma–Aldrich), 1 μM N-acetylcysteine (Sigma–Aldrich), and 10 μM Y27632 (Stemgent). Added to the single cell suspension was 1 ml FBS and 3 ml advanced DMEM/F12, before passing through a 40 μm filter to remove multicellular aggregates. The ISC pellet was formed by centrifugation at 1200 RPM for 4 min. The cell pellet was resuspended in an appropriate volume of media and 10 μl of the suspension was added to the surface of the patterned Matrigel gel. Cell-laden gels were incubated at 37 °C and 5% CO_2 for 15 min before carefully adding 600 μl of growth media (ENRCV) supplemented with blebbistatin (15 mM) to each well. Media was replaced with ENRCV, but without blebbistatin two days after seeding.

2.14. Immunofluorescence analysis

Three days after seeding, ISC monolayers were fixed with 4% paraformaldehyde and 0.1% glutaraldehyde in PBS (15 min, room temperature). Following fixation, gels were washed with PBS (3 × 10 min at room temperature), treated with 20 mM sodium borohydride in PBS (5 min, room temperature), and washed again with PBS (3 × 10 min, room temperature). The gels were then solubilized using 0.2% triton X-100 in PBS (1 h at room temperature) and blocked using 10% horse serum and 0.01% triton X-100 in PBS (1 h, room temperature). The samples were then incubated overnight at 4 °C with rhodamine phalloidin (1:200) and DAPI (1:2000) in blocking buffer. After washing with PBS (5 × 1 h, 4 °C) to remove any residual antibody, the fluorescently labeled monolayers were imaged using confocal microscopy (Zeiss LSM 710).

2.15. Frequency map generation

Z-stack images were taken of ISCs fixed and stained for the nucleus and actin cytoskeleton after 3 d of culture on microwell patterned matrigel substrates. The locations of cell nuclei along the top, middle, and bottom, of the patterned microwell structure were determined using ImageJ. Nuclei within the lower 20 μm and upper 20 μm of the stack were counted

as the 'bottom' and 'top', respectively, while the intermediate stacks were considered the 'middle'.

Coordinates of individual nuclei were normalized to the center of each well and scaled to the measured radius of each well. Cell data were then assembled in MATLAB and displayed using the pcolor() function.

3. Results

3.1. Design of degradable thioester crosslinked PEG elastomers

The photoinitiated thiol-ene 'click' reaction (scheme 1) is known to drive rapid formation of a step-growth network while exhibiting favorable characteristics, such as high selectivity, allowing for use in combination with other functional groups, cytocompatibility, and insensitivity to oxygen [36]. In recent literature, the photoinitiated thiol-ene polymerization has also been used to produce crosslinked materials with dynamic thioester crosslinks for applications ranging from the design of viscoelastic hydrogels to recyclable thermosets [25, 26, 37].

In this work, thioester elastomers were synthesized from thiol and thioester norbornene functionalized PEG macromers. Specifically, the thiol macromer was synthesized by thiolation of a three-arm 1 kDa PEG alcohol (>95% functionalization by ^{1}H NMR) by Fischer esterification with 3-mercaptopropionic acid (figure 1(a)). The thioester norbornene macromer was synthesized by further functionalization of the thiol macromer with 5-norbornene-2-carboxylic acid to yield a thioester norbornene functionalized macromer (∼85% functionalization by ^{1}H NMR, figure S1).

Thiol and thioester norbornene macromers were combined in a 1:1 ratio of thiol to norbornene and mixed with a concentrated solution of LAP photoinitiator in water (82.6 mg ml^{-1}, 0.01eq LAP) to form a final solution that was 97.1 wt% polymer and yielded an elastomeric network when cured with 356 nm UV light (10 mW cm^{-2}, 15 min). Mechanical properties of the thioester elastomers were measured using an RSA-G2 DMA (TA Instruments). Thioester elastomers exhibit a young's modulus (E) of 2.6 ± 0.4 MPa, ultimate tensile strength of 1.8 ± 0.2 MPa, and a strain at break of 160% ± 50% (figure 1(b)). Young's storage modulus and tan(delta) measurements were conducted over a temperature range of −70 °C to 30 °C, and a glass transition temperature of −40 °C was observed (figure 1(c)). The degradation of the elastomers was assessed under slightly basic conditions with a high concentration of thiol (pH 9.0, 300 mM 2-mercaptoethanol), consistent with a thioester exchange mechanism as reported previously [28, 29]. Over the course of 2 h, transparent, dimensionally stable elastomer samples became tacky and opaque, eventually degrading into a viscous residue (figure 1(c)).

3.2. PEG thioester elastomers degrade rapidly in 2-mercaptoethanol with little swelling

Thioesters undergo nucleophilic attack by a deprotonated thiol (thiolate), leading to a rearrangement and the formation of a new thioester and the regeneration of a thiolate (scheme 2).

This reaction is reversible and has been well studied in both hydrogel and elastomer systems, including exchange reactions that lead to degradation [25, 37]. In the case when a monofunctional thiol is introduced to the thioester network, thioester exchange results in the cleavage of crosslinks and subsequent mass loss. To better understand how crosslink cleavage via thiol catalyzed thioester exchange gives rise to mass loss in the three-arm PEG system developed here, thioester elastomer samples were immersed in a basic aqueous buffer (pH 9.0 100 mM tris buffer) with and without 300 mM 2-mercaptoethanol. Samples were monitored with degradation time until complete mass loss (<2 h).

To better understand the degradation mechanism and alterations in the network structure with time, rheological properties were measured on the thioester elastomers as a function of degradation. When thioester elastomers were placed in a pH 9.0 solution with thiol, the shear elastic modulus (G') decreased exponentially with time until complete degradation (figure 2(a)). Moduli data were normalized to the initial swollen shear elastic modulus (G'_o) and fit to the exponential decay function $\frac{G'}{G'_o} = \exp\left(-\frac{t}{\tau}\right)$ where t is time and the characteristic degradation time τ was determined to be 17.9 ± 0.3 min (figure S4). This result suggested to us a relatively uniform crosslink cleavage throughout the sample, typical of a bulk degradation process. However, it is important to note that erosion/mass loss is dictated by the network connectivity and solubility of the degraded fragments. As a control, thioester elastomers displayed no significant change in modulus over the course of 2 h in pH 9.0 solution without thiol, suggesting no crosslink exchange. Thus, on the time scale of these experiments, hydrolysis of the network ester groups is negligible, and elastomer degradation is occurring primarily through thiol thioester exchange.

At selected time points, samples were lyophilized and mass loss over time was quantified. No significant mass loss was observed for thioester elastomers placed in media without thiol, however, in media with thiol the thioester networks exhibited a linear mass loss at early times points and 93% ± 7% of the initial polymer mass remained in the thioester condition at 1.5 h (figure 2(b)). Equilibrium mass swelling data show and increase in the swelling of thioester networks in thiol solution from 1.8 ± 0.3 g g^{-1} to 2.4 ± 0.2 g g^{-1} over 1.5 h of degradation (figure 2(c)). While this is an appreciable change in swelling, the small magnitude compared to the 100 fold change in shear elastic modulus suggest swelling was not strongly affected

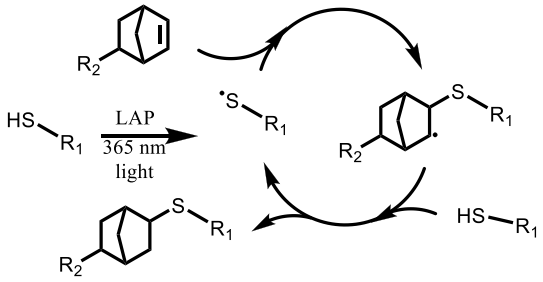

Scheme 1. The photoinitiated thiol-ene 'click ' reaction catalyzed with LAP and 365 nm light.

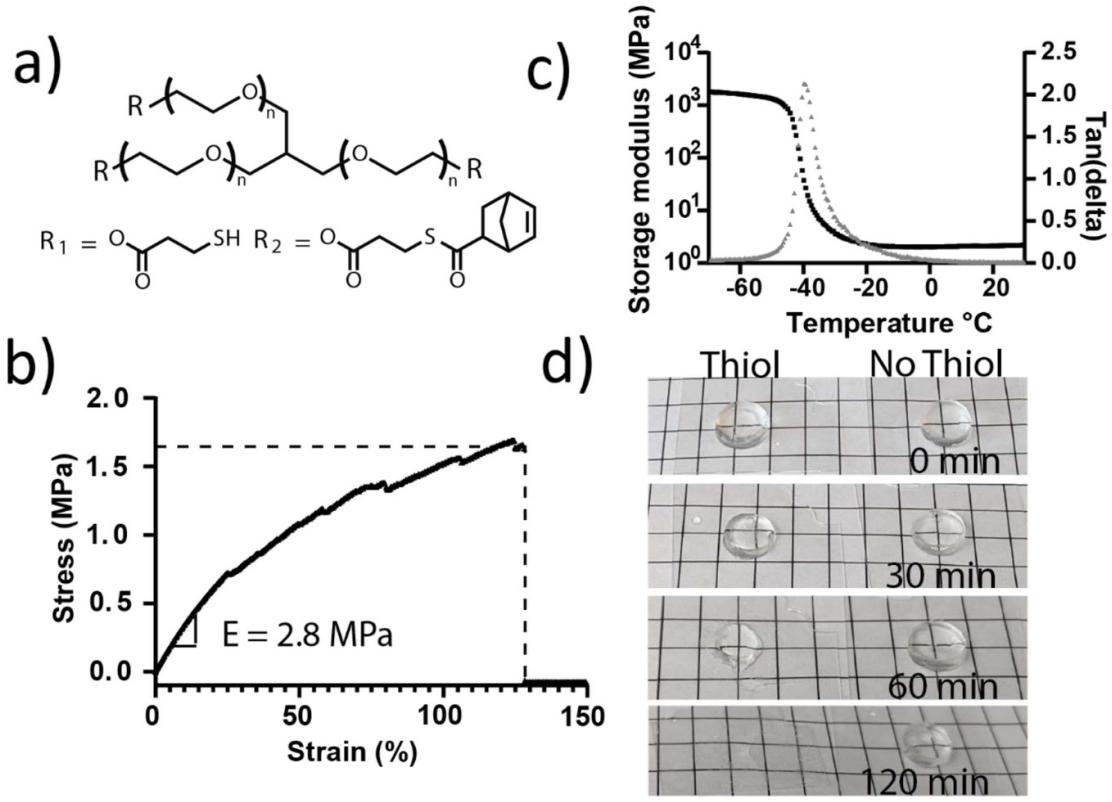

Figure 1. Photoinitiated thiol-ene 'click' chemistry and thioester chemistry were used to create mechanically robust networks with adaptable crosslinks. (a) A three-arm PEG macromer was functionalized with thiol or thioester norbornene function groups to yield resin precursors: three-arm PEG thiol (1300 Da) and three-arm PEG norbornene with internal thioester groups (1600 Da). (b) Typical stress–strain behavior of a thioester elastomer under tensile loading until failure (0.1 mm s^{-1}). The Young's modulus was calculated using the slope of the curve between 5% and 10% strain. (c) The young's storage modulus (black) and tan(delta) (grey) were measured as a function of temperature. A glass transition temperature of −40 °C is illustrated by the position of the peak in tan(delta). (d) Representative images of free-standing elastomer samples placed in pH 9.0 tris buffer over the course of 2 h with and without 300 mM 2-mercaptoethanol to monitor degradation. Gridline spacing is 5 mm.

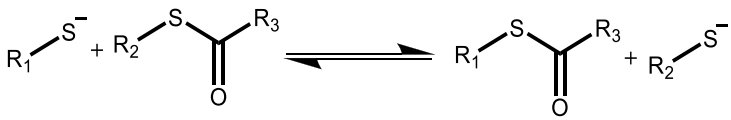

Scheme 2. Thioester exchange is catalyzed by the presence of deprotonated thiols and results in new thioester and regenerated thiolate anion.

by the degradation. These non-swelling characteristics are known to occur in water swollen networks with decreased hydrophilic character either though high crosslink densities [30, 38] or the addition of less hydrophilic polymers often with thermoresponsive character [30, 39].

Macroscopically, this combination of polymer swelling increasing by a factor of 2 and 3, while *G*

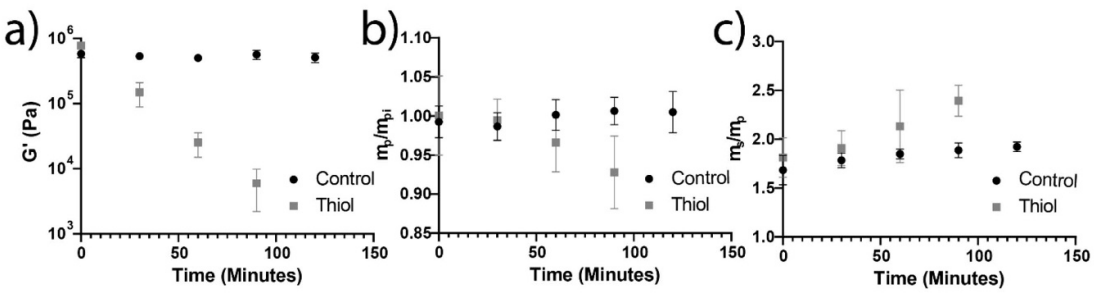

Figure 2. Degradation of thioester elastomers placed in pH 9.0 buffer with and without 300 mM 2-mercaptoethanol was observed over 2 h. Degradation was only observed when 2-mercaptoethanol was present in solution suggesting degradation was mediated only by thioester exchange. (a) Shear swollen moduli were observed as a function of time. An exponential decrease in modulus was observed for the thiol condition suggesting that crosslinks were cleaved throughout the sample via a bulk erosion mechanism. 0.1% strain, 1 Hz; $N = 3$, error bars are standard deviation. (b) Elastomer samples were lyophilized measured for polymer mass. Dry mass data were normalized to the calculated theoretical amount of polymer included in formulation and plotted here as a function of time and degradation condition. $N = 3$, error bars are 95% confidence interval. (c) Mass swelling ratio was calculated as the ratio of the swollen polymer mass to the measured dry mass and are reported here as a function of time and degradation condition. $N = 3$, error bars are 95% confidence interval.

changes by two orders of magnitude resulting in a slow transition from clear rigid solid to viscous liquid without large changes in sample dimensions with the simple introduction of 2-mercaptoethanol. This is highly advantageous for cast-mold applications where large amounts of swelling typically observed in degrading hydrogel systems could damage cast features. The concept of a thiol stimulus to induce degradation in a 3D printable resin rendered this formulation suitable for the goal of printing sacrificial molds.

3.3. DLP printing of thioester elastomers to produce high-resolution 3D structures with overhanging features

To print thioester elastomers and assess the resolution and critical dimension limits of the thioester materials, a high-resolution DLP printer was used. Uniform illumination was achieved using a 1920 × 1152 pixel liquid crystal on silicon SLM with 405 nm light to form the desired image from a digital file that was then de-magnified to the sample plane (figure 3(a)). The extinction ratio for this SLM was 99.3%. A non-stick PDMS on glass window was illuminated from underneath the sample for a bottom-up build direction upon the print stage, and the stage was moved vertically to create each layer. Each layer was exposed with a unique image before raising the print stage; additional resin then flowed into the exposure plane; and the next layer was exposed to a new image.

To print thioester resins, the three-arm PEG thiol and three-arm PEG thioester norbornene macromers were added to a concentrated LAP solution to form a solution that was 97.1 wt% polymer with a molar ratio of thiol:norbornene:LAP of 1.1:1.0:0.011, respectively. The formulation was modified to include a 10% excess of thiols, which was found to improve bonding between printed layers, presumably due to the ability of unreacted thiols to participate in the thiol-ene polymerization of the subsequent layer. FTIR was used to monitor the disappearance of peaks associated with the thiol (2555 cm^{-1}) and norbornene (714 cm^{-1} and 3060 cm^{-1}) functional groups when irradiated with 8 mw cm^{-2} 405 nm light (figure 3(b)). The initial slope of each conversion plot was measured in the initial linear region of the plot and found to be 0.066 ± 3 s^{-1} for thiol species and 0.070 ± 4 s^{-1} for norbornene species; this suggests thiol and norbornene species were consumed at a 1:1 rate. As expected, the norbornene conversion was higher than the thiol conversion due to the 10% thiol excess in the resin formulation with values of 0.97 ± 0.04 and 0.91 ± 0.03 respectively. 30 s of 8 mw cm^{-2}, 405 nm light was selected as the minimal dose necessary for a full cure.

To facilitate the printing of layers, a photoabsorbing species was added to the formulation to attenuate light and control the depth of penetration. Cure depth calculations were conducted as previously reported [40], but briefly, Beer–Lambert absorption was assumed for the photoabsorber (Tinuvin Carboprotect, BASF) then combined with the light dose-conversion profile determined by FTIR, and the percolation threshold of 50% conversion for a three-arm three-arm step growth co-polymerization to determine the maximum depth where light could penetrate and form a gel. At a concentration of 0.75 wt% Tinuvine Carboprotect, 90% of light was absorbed in the top 110 μm of the resin, and for a single 30 s exposure at 8 mW cm^{-2}, 405 nm light the cure depth was determined to be 50 μm. Importantly, this means that the z-dimensions of overhang features, since light was patterned on liquid resin with no previous layers,

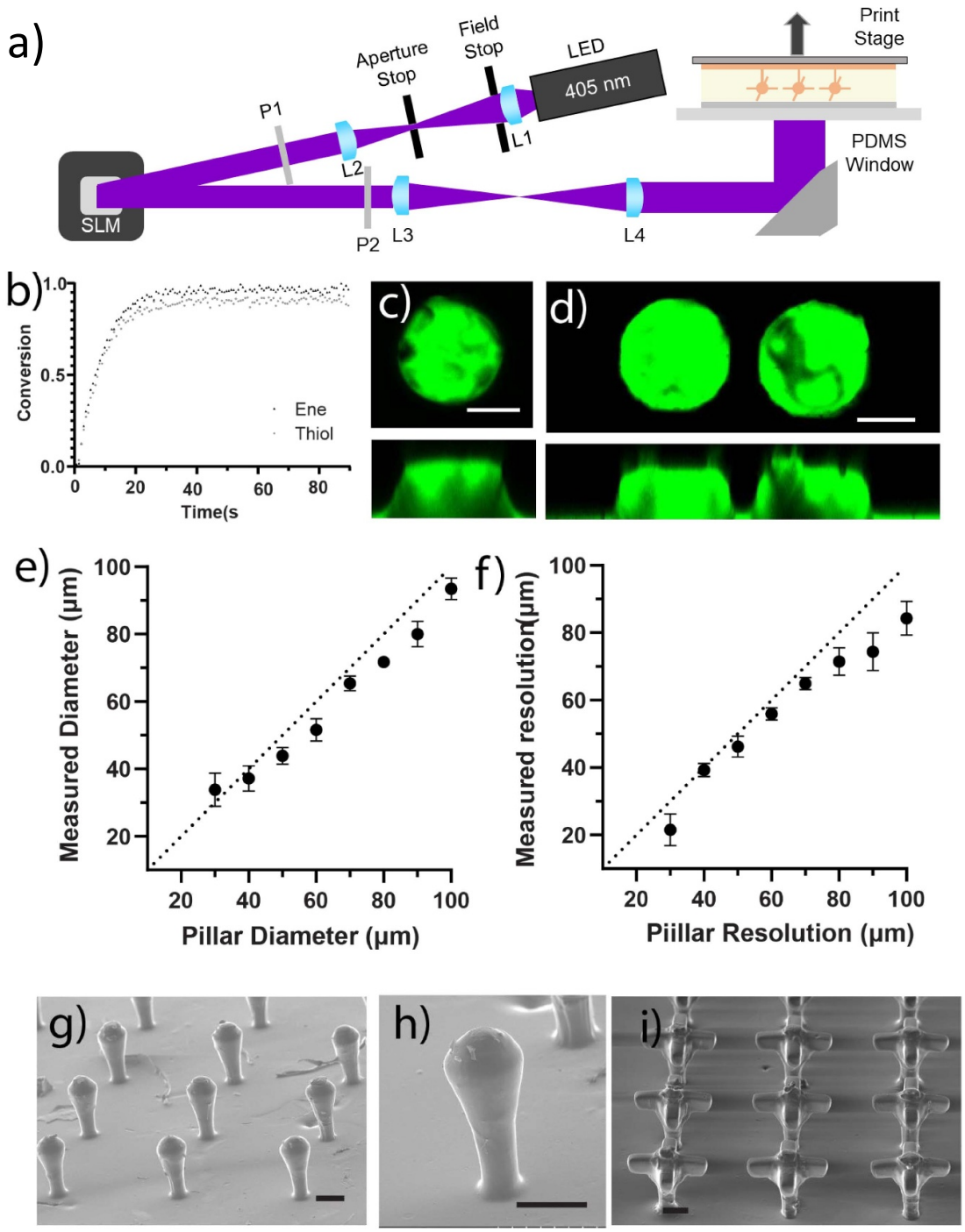

Figure 3. Thioester elastomer photocurable resins were optimized for printing with existing high resolution DLP 3D printing techniques. (a) Schematic of DLP 3D printing stage and process. Lenses and polarizers are labeled L and P, respectively, and the spatial light modulator is labeled 'SLM'. (b) FTIR spectroscopy was used to obtain conversion of norbornene and thiol species as a function of light dose delivered to the sample. (8 mW cm^{-2}, 405 nm light, $N = 3$). (c) Top and side view of a single 50 μm tall, 100 μm diameter pillar, and (d) a pair of pillars patterned 30 μm apart. Elastomer stained with fluorescein. Scale bars 25 μm. (e) Measured pillar diameter plotted versus patterned diameter, a dotted line with a slope of 1 is plotted for visual reference. $N = 3$ stamps each containing three technical replicates averaged together, error bars are standard deviation. (f) Measured pillar spacing plotted versus patterned pillar spacing. A dotted line with a slope of 1 is plotted for visual reference. $N = 3$ stamps each containing three technical replicates averaged together, error bars are standard deviation. SEM was used to take images of three dimensional constructs containing overhang features including: arrays of (g) and (h) crypt and (i) branched crypt structures. Scale bars 100 μm.

were determined by the cure depth rather than the layer thickness set by the stage. To account for this effect, overhang feature designs were adjusted based on the calculated cure depth (figure S5). At these printing conditions, a layer thickness of 10 μm optimized the fidelity of the x–y features while ensuring layer-to-layer adhesion and printing of reliable 3D structures.

Once the printing process and formulation were optimized, the critical dimension and resolution limits of the printing platform were tested. To analyze these parameters, features of various sizes and varied spacing were printed onto prefabricated 100 μm thick thioester elastomer bases, which acted as a stamp-like support when manipulating the printed constructs (figures 3(c) and (d)). Critical dimensions were assessed by printing 50 μm tall cylinders with diameters ranging from 30 to 100 μm (figure S6). For characterization purposes, printed constructs were stained with fluorescein (acid yellow 73), and directly imaged via laser scanning confocal microscopy. Measurements of the pillar diameter were taken between 10 and 20 μm from the top of the pillar to avoid the influence of surface distortions, thus, printed structures that did not exceed a height of 20 μm were not measured (figure 3(e)). The experimental limits of patterned resolution were assessed in a similar fashion where two cylinders 50 μm tall and 100 μm in diameter were printed at spacings ranging from 10 to 100 μm. For these experiments, measurements were taken between 10 and 20 μm from the top of the pillars, and we observed a minimum resolution of 30 μm (figure 3(f), S7). Interestingly, both the measured diameter and resolution of the patterns were slightly smaller than the designed dimensions. This difference might be attributed to elastomer shrinkage during the ethanol washes or after desiccation (see 3D printing thioester elastomers in section 2).

The results of 2D characterization of minimum critical dimensions and feature sizes were used to design a series of 3D structures with overhang features ranging from slight to extended protrusions. Many of the printed structures were selected to be reminiscent of the crypt and/or branched crypt structures found in the intestinal epithelium (figure 3(g)). The achievement of these crypt-like structures demonstrates the resolution achievable with this material system and the ability of the method to create molds with overhanging features (figures 3(g) and (h)). Figure 3(i) shows distinct overhangs with features sizes down to 50 μm in the *x*, *y*, and *z* print directions; these structures and size scales were similar to other fabricated branched crypt structures (figures 3(h) and (i)) [10, 17]. These results show, however, that rounding occurs at the edge of features which has been previously observed [40]. We attribute this artifact to polymerization in the 'dark' region as a result of simultaneous reaction and diffusion that occur when printing and patterning features near the resolution limit of the material [41].

3.4. Hydrogel substrate influences feature size, resolution, and depth

After characterizing the limits of printed features and resolution, we next sought to understand how printed patterns transferred to soft synthetic (PEG hydrogel) and extracellular matrix (Matrigel) platforms relevant to the culture of intestinal organoids. The PEG hydrogel was composed of eight-arm 20 kDa PEG norbornene and two-arm 5 kDa PEG thiol combined in a stoichiometric ratio diluted to 2 wt% ($G' = 740 \pm 50$ Pa, figure S2), which compares favorably with PEG hydrogel organoid culture platforms [6]. To pattern soft hydrogels, elastomer stamps were brought into contact with pre-gel mixture, and gelation was induced by placement of the sample the incubator (Matrigel) or irradiation with 365 nm light (PEG hydrogel). Once the hydrogel cured, the elastomer hydrogel complex was immediately bathed in 100 mM tris buffer supplemented with 300 mM 2-mercaptoethanol adjusted to a pH of 9.0.

To quantitatively characterize how the printed thioester features patterned into the hydrogels, the final pattern critical dimension, resolution, and depth were measured in Matrigel and PEG hydrogels (figure 4(a)). Measurements of pillar diameter and spacing were once more assessed between 10 and 20 μm of the bottom of the well in order to most closely match the diameter of the pillar section used to cast the well. Well depth measurements were measured to the nearest whole image slice of a *z*-stack taken of each well (figures 4(b)–(d)). Analysis of the patterned well diameter data revealed that critical dimensions were a function of the type of material with 40 and 60 μm pillars being the smallest size of pillars that could be transferred into the PEG and Matrigel hydrogels, respectively (figure 4(e)). At the largest condition patterned well sizes for both hydrogel platforms were larger than the original pattern by ~30% (e.g. $D_{mold} = 93 \pm 3$ μm vs $D_{well} = 118 \pm 16$ μm).

Opposite trends were observed for patterned resolution in the PEG versus Matrigel hydrogels. The spacing between patterned wells in the PEG hydrogels followed a slope slightly higher than one (1.27 ± 0.10), suggesting the spacing between wells grows larger by an amount proportional to the original patterned distance (figure 4(f)). This observation is consistent with the isotropic expansion expected as the cast hydrogel reaches equilibrium swelling in PBS [42, 43]. In contrast, the space between the wells in Matrigel mostly contracted, with the smallest patterned gap of 40 μm measuring only 16 μm. Instead of a change in slope of measured well gap plotted against measured pillar gap, we observe a downward shift in the *y*-intercept. This suggested

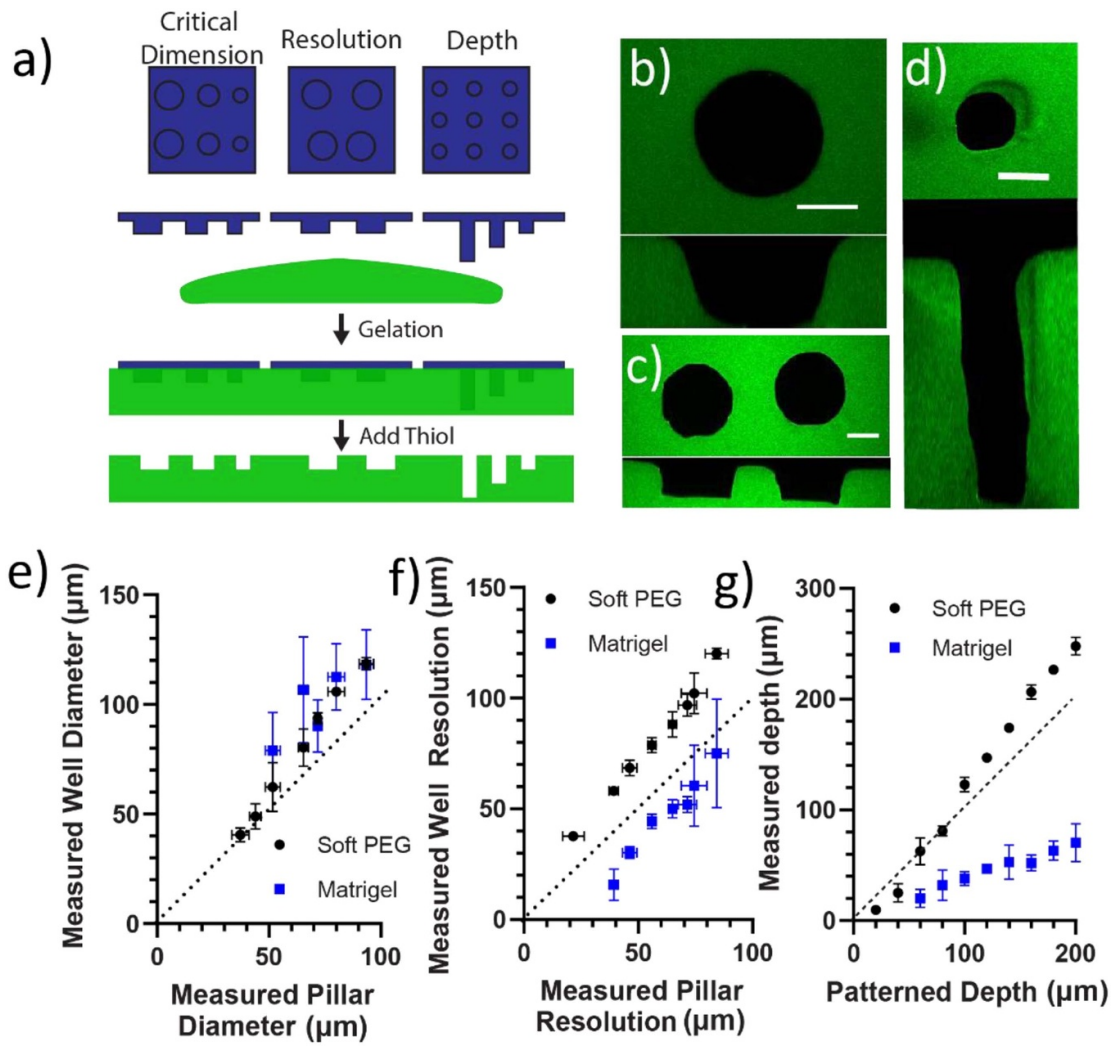

Figure 4. Thioester elastomer structures were degraded *in situ* to cast patterns into soft, swollen hydrogel platforms. (a) 3D printed thioester elastomer constructs were lowered into solutions of Matrigel or eight-arm 20 kDa PEG norbornene and two-arm 5 kDa PEG thiol combined in a stoichiometric ratio diluted to 2 wt% ($G' = 740 \pm 50$ Pa). Each hydrogel was polymerized, then a solution of pH 9.0 300 mM 2-mercaptoethanol was added to degrade the thioester elastomer stamp. Hydrogel cast patterns were then equilibrium swollen in PBS and imaged by laser scanning confocal microscopy to assess how printed pillar dimensions transfer to each hydrogel substrate. (b) 50 μm tall pillars with a range of diameters were patterned into Matrigel and soft PEG hydrogels. *Z*-stack images of each well were taken with laser scanning confocal microscopy. Well diameter was measured between10 and 20 μm from the bottom of the well using MATLAB (for more details please see section 2). A representative image is shown of a well cast by a 90 μm diameter pillar into PEG hydrogel. An orthogonal view of the *XZ* plane is included for reference. (c) 50 μm tall, 100 μm diameter pillars with a range of spacing were patterned into Matrigel and soft PEG hydrogels. *Z*-stack images of each well were taken with laser scanning confocal microscopy. Well resolution was measured between 10 and 20 μm from the bottom of the well using MATLAB (for more details please see section 2). A representative image is shown of a pair of wells cast by pillars 30 μm apart into PEG hydrogel. An orthogonal view of the *XZ* plane is included for reference. (d) 50 μm diameter pillars with a range of printed heights were patterned into Matrigel and soft PEG hydrogels. *Z*-stack images of each well were taken with laser scanning confocal microscopy. Well depth was measured as the number of image slices multiplied by the image thickness (for more details please see section 2). A representative image is shown of a well cast by a 200 μm tall pillar into PEG hydrogel. An orthogonal view of the *XZ* plane is included for reference. (e) The measured well diameter in Matrigel and soft PEG hydrogels is plotted versus the measured pillar diameter in the elastomer print. (f) The measured well separation in Matrigel and soft PEG is plotted versus the pillar separation measured for the elastomer print. (g) The measured well depth in Matrigel and soft PEG is plotted versus the designed height of the elastomer print. PEG hydrogels were visualized by 2000 kDa FITC dextran entrapped in network. Scale bars 50 μm. $n = 3$ patterned hydrogels each containing three technical replicates averaged together.

to us that the observed effect is likely not a function of the measured distance between pillars, but rather a property of the Matrigel itself.

Finally, we explored the depths of the patterned wells as a function of pillar height. Given that the print height was controlled by the layer-by-layer printing process, the patterned well depth was compared directly to the patterned pillar height. Patterned wells in PEG hydrogels were slightly deeper with a 200 μm pillar forming a 248 $\pm$ 8 μm deep hole (figure 4(g)). This enlargement was proportional to the height of the initial pattern with a slope greater than one indicative of hydrogel swelling. In contrast, the wells in Matrigel were shallower; the sample 200 μm pillar formed a 70 $\pm$ 17 μm deep well. This contraction was proportional to the height of the original pattern

with a slope less than one indicative of hydrogel contraction.

Overall, patterns transferred into PEG reflect the original pattern with high fidelity, albeit with a predictable enlargement of critical dimension, resolution, and depth consistent with isometric expansion. We hypothesize that pattern trends in Matrigel are consistent with isometric contraction of a viscoplastic hydrogel. Since the designed thiol solution has a high concentration of thiol and tris buffer, sudden introduction to the soft hydrogels may cause a sudden isometric contraction on the timescale of the diffusion of water out of the hydrogel and salts and thiol into the hydrogel. The thioester elastomer has a higher modulus and, therefore, would not undergo the same amount of isometric contraction, potentially causing compressive stress to build up around the imbedded pattern. Matrigel, as a known viscoplastic hydrogel, would relax the imposed stress around the elastomer features through network rearrangement [44]. This may explain why the diameter of patterned holes enlarge while other metrics show contraction. These same trends were not observed in PEG hydrogels, as PEG hydrogels are poroelastic materials; compressive load over time results in the movement of water out of the hydrogel but no plastic deformation [45].

3.5. Thioester fabrication facilitates formation of close patterned and overhanging structures in Matrigel

After characterizing the effect of the material chemistry on the final printed features' dimensions and resolution, we next investigated the ability of the sacrificial thioester mold to transfer close-patterned and overhanging features embedded within Matrigel (figure 5(a)). The current *in vitro* model of the intestinal organoid is a spherical cyst structure (∼100–200 μm in diameter) with crypt-like buds where the stem cells reside. To template the size of the intestinal organoid cysts, we fabricated a close-packed, 5 × 5 array of 150 μm tall stems that were 50 μm in diameter and space 50 μm apart, and then printed a 150 μm sphere on the top of the stem (figure 5(b)). The thioester elastomeric mold was pressed into Matrigel and subsequently degraded. Using a laser scanning confocal microscope, tile images were collected at the top and middle of the features patterned within Matrigel (figures 5(c) and (d)). Consistent with prior results, the patterned well dimensions in Matrigel were enlarged compared to the original 3D printed elastomer mold, with the stem portion of the well enlarging from 62 ± 3 μm to 143 ± 5 μm, and the ball portion enlarging from 130 ± 2 μm to 203 ± 4 μm (figure 5(e)). Similar to trends reported in figure 4, the space between features contracted compared to the original printed construct with crypt–crypt distances reducing from 52 ± 3 μm to 41 ± 2 μm and opening–opening distances reducing from 122 ± 5 μm to 106 ± 5 μm. The feature depth was also reduced from 227 ± 8 μm to 84 ± 2 μm.

Next, PEG thioester sacrificial molds were fabricated with similar dimensions, but including 100 μm long, 50 μm tall and 50 μm wide branched, channels to template the stem cell crypt niches (figure 5(f)). After degradation, images taken at the surface and middle of the patterned Matrigel once more showed enlarged and slightly misshapen branched structures (figures 5(g) and (h)). Nevertheless, distinct overhang void spaces with high aspect ratios were formed in Matrigel (figure 5(i)).

3.6. ISCs form epithelial layers conforming to 3D patterned features

ISCs encapsulated in Matrigel grow to form cyst-like enteroids and upon differentiation and self-organize to form multicellular intestinal organoid where paneth and ISCs reside in the budded crypt regions. When ISCs are cultured on 2D patterned substrates, they proliferate to form a confluent epithelial cell monolayer, where the cell sheet layer conforms to the underlying features of the of the tissue culture substrate. Here, to recapitulate the dimensions of mouse intestinal villi and crypt structures [46], we first printed pillars that were 50 μm in diameter and 200 μm in height using the thioester formulation. The sacrificial mold was then used to transfer the intestinal features into Matrigel, forming wells 104 ± 4 μm in diameter and 72 ± 2 μm deep (figure S8). Finally, ISCs were seeded in the patterned Matrigel structures. After 24 h, a monolayer of the epithelial cells forms at the base of the wells, and over times, the ISC begin to migrate towards the gel surface (figure 6(a)). By 72 h, a confluent monolayer of epithelial cells forms on the hydrogel surface. Samples fixed after 72 h and stained for F-actin and cell nuclei showed complete coverage of a confluent monolayer that conformed to the top, sides and bottom of the patterned well geometries with nuclei interspersed throughout (figure 6(b)). Monolayer confluency can be additionally visualized through a *xz*-projection, shown in supplementary figure S8(d). *Z*-stack images were used to identify the location of cell nuclei along the top, sides, and bottom, of patterned microwells. Nuclear coordinates were scaled to the measured radius of each well, and a frequency map was plotted with MATLAB (figure 6(c)). Similar frequencies of cell nuclei were observed at the top, middle, and bottom, of the well structure suggesting that after ISCs underwent proliferation and migration out of the wells, a uniform distribution of cells was reached in the final confluent layer.

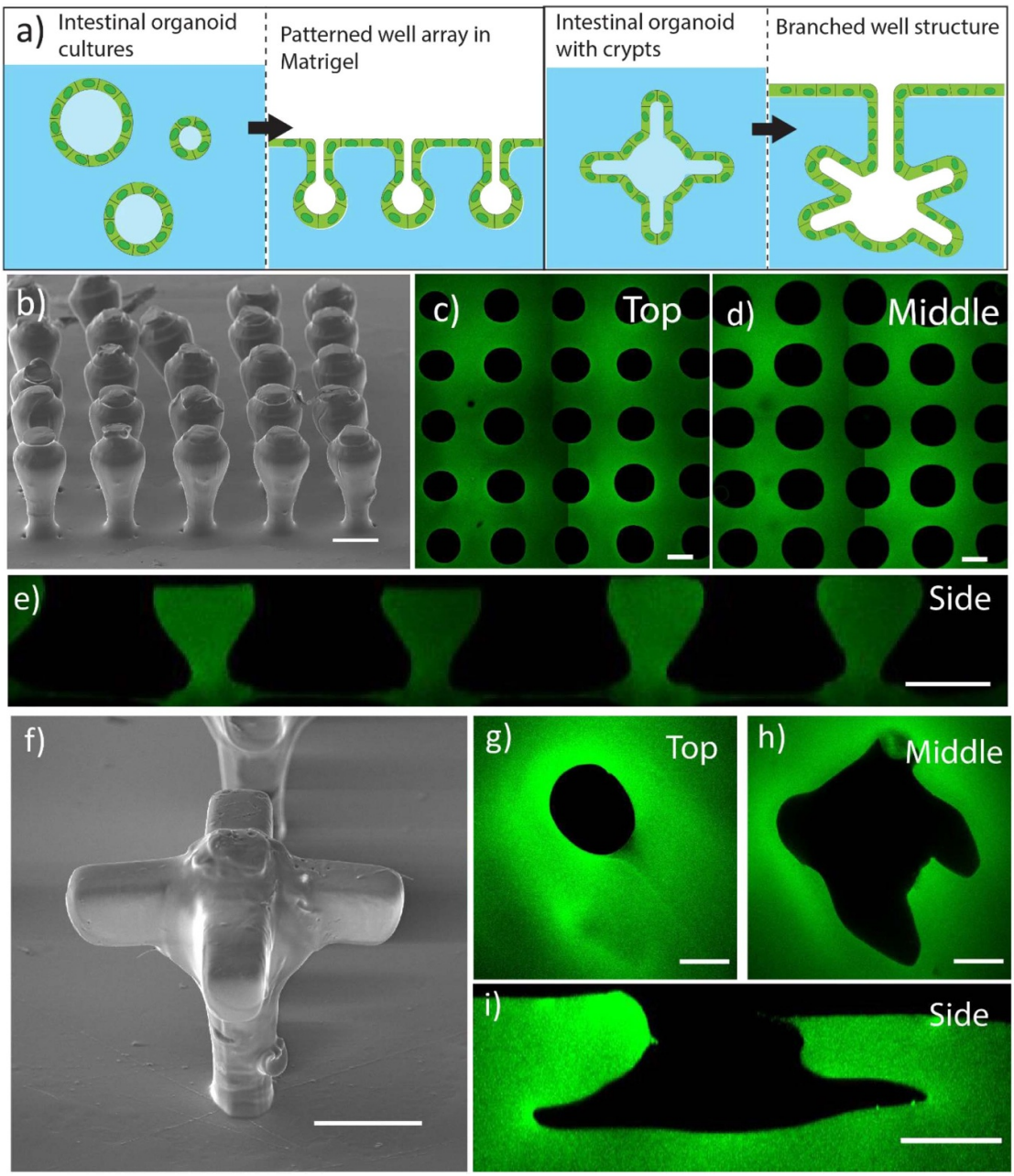

Figure 5. (a) Printed thioester features were reproducibly degraded in the presence of Matrigel to cast mold close-packed and overhanging structures reminiscent of the intestinal organoid features. (b) SEM image of printed crypt structures consisting of a 150 μm ball on top of a 50 μm wide by 150 μm tall stem printed with a 50 μm spacing. Scale bar 100 μm. Printed organoid features were patterned into Matrigel and a tile scan was taken of the (c) stem and (d) ball regions of the well. (e) *Z*-stack images of each well were taken with laser scanning confocal microscopy and used to construct an orthogonal view of the patterned array along the *XZ* plane. Scale bar 100 μm. (f) SEM image of branched crypt structure shows defined overhang features. Scale bar 100 μm. Printed organoid features were patterned into Matrigel and images were taken of the (g) stem and (h) branched crypt regions of the well. (i) *Z*-stack images of each well were taken with laser scanning confocal microscopy and used to construct an orthogonal view of the patterned array along the *XZ* plane. Scale bar 100 μm. Matrigel hydrogels were labeled with FITC fluorophore after patterning. For more details, please see patterned hydrogel staining and image analysis in section 2.

4. Discussion

With the growing applications and interest in intestinal organoids, there is a heightened appreciation as to the role of microenvironmental factors, especially those that affect cell shape and final organoid geometry, on the final structure of the differentiated organoid [7, 47]. High resolution 3D printing techniques, such as DLP, can generate free-standing crypt and villi structures relevant to the intestinal organoid (<100 μm), but usually require printing resins >100× stiffer than Matrigel, which is used for ISC cultures. Sacrificial 3D printing techniques have been used to pattern complex 3D geometries in otherwise less printable hydrogels like Matrigel [13], but a lack of photopolymerizable resins that degrade rapidly under mild conditions compatible with Matrigel has hindered the translation of

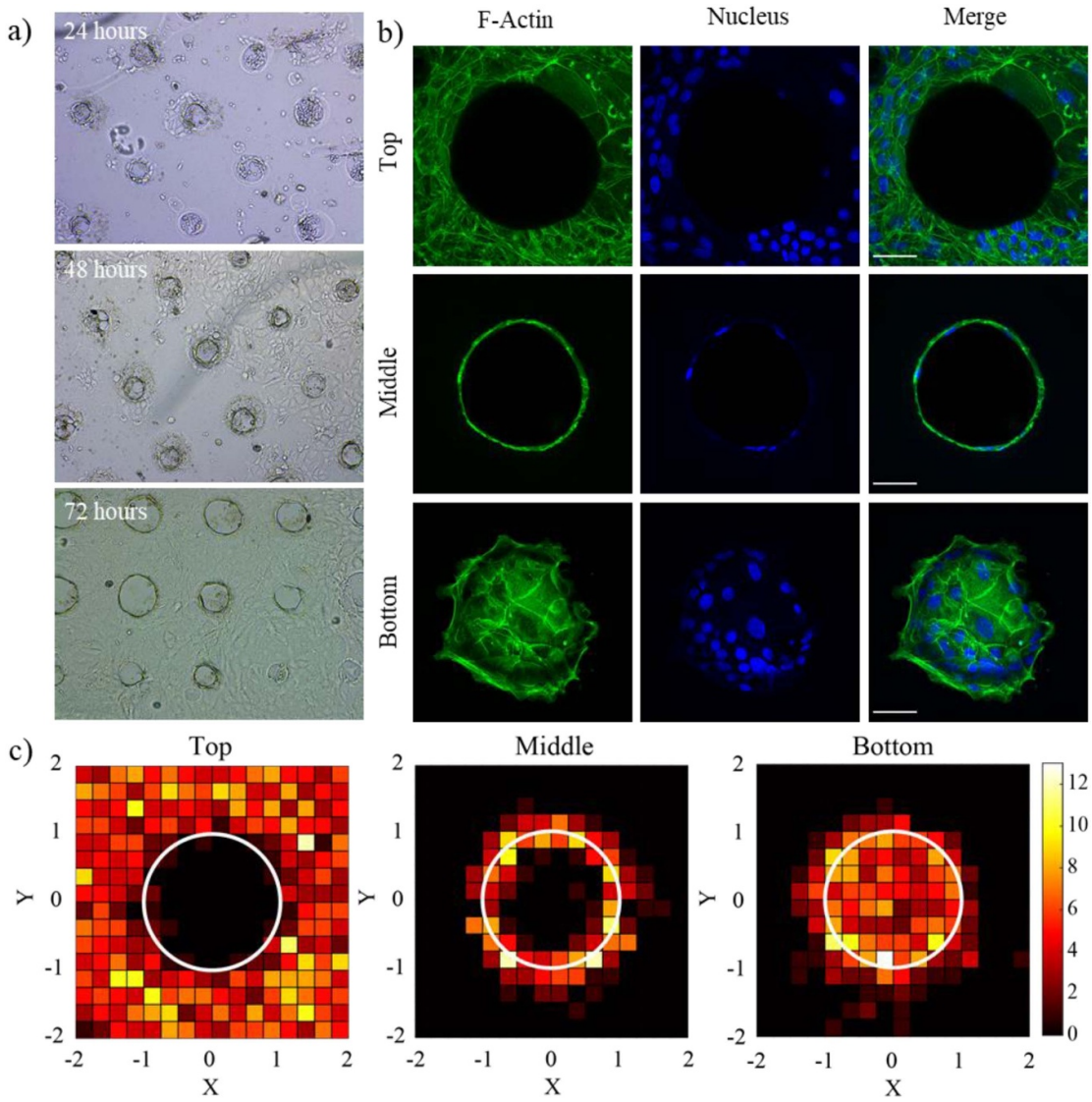

Figure 6. (a) Single ISCs were seeded onto patterned Matrigel gels and formed confluent monolayers over the course of 3 d. (b) Immunostaining for F-actin (green) and nuclei (blue) shows the formation of a cell monolayer covering the patterned features. Scale bar is 50 μm. (c) Frequency map images representing nuclear placement of ISCs along the top, middle, and bottom, of each well show even dispersion along the surfaces of the patterned well structures. *X* and *Y* image dimensions were normalized to the radius of each microwell which is represented by a white circle. The color bar represents the number of nuclei present in each region. $N = 20$ wells.

sacrificial approaches to light-based 3D printing systems. To address these issues, we developed a photocurable PEG thiol-norbornene elastomer with thioester function groups on the backbone to facilitate network erosion. A high concentration of thiol (2-mercaptoethanol) and mild basic conditions (pH 9.0) were selected to drive trans-thioesterification of 2-mercaptoethanol with thioester crosslinks and balance gentile degradation conditions with fast degradation times (<2 h). These photocurable PEG thioester resins readily translated to existing high-resolution DLP 3D printing platforms where critical dimensions of 37 $\pm$ 4 μm and resolutions of 22 $\pm$ 5 μm were achieved.

One limitation of the thioester sacrificial patterning in this work is that while degradation conditions are gentle enough to maintain integrity of soft tissue culture substrates, the use of a non-physiological pH precludes the presence of cells during elastomer erosion. This is an important limitation compared to other light [22] and extrusion [13, 15] based sacrificial printing strategies, where cytocompatible fabrication strategies easily facilitate the creation of cocultures by culturing one cell type in the hydrogel substrate, and another cell type in the degraded construct. In this work, the elevated pH was used to accelerate degradation by increasing the amount of deprotonated 2-mercaptoethanol. Although pH exerts a potent influence on thioester exchange, other factors such as pKa of the thiol and thioester could be used to achieve similar rates of degradation at more physiological pH values. To facilitate fabrication in the presence of cells a thioester resin could be made with a lower pKa thiol and degraded with a molecule

like cystine which is cytocompatible and readily forms thiolate species at physiological pH.

While the ~10 μm dimension and resolution limits that are achievable with photoablative techniques remain unmatched for patterning biological materials [17, 18], the DLP printed degradable thioester materials provide a complementary biofabrication method that provides the attainment of cellularly-relevant feature sizes with rapid printing of large arrays of features. Results (e.g. figure 4(e)) demonstrated that thioester sacrificial molding allow feature sizes >40 μm in soft cell culture substrates, which compare favorably to commonly used PDMS micromolding [34, 35]. However, the on-demand degradation of the thioesters and tailoring of the material properties offers additional benefits for creating features embedded within soft hydrogels and the ability to fabricate interconnected and overhanging features. We further demonstrate these overhanging features can be printed close together to form dense arrays with resolutions as small as 40 μm and that the overhangs can be patterned in Matrigel with either low or high aspect ratios. In addition, branched structures, extending >100 μm into the culture substrate, from primary culture well were created . Since each layer is printed with a single light exposure, DLP 3D printing techniques provide the ease of scalability and speed compared to photoablative techniques, where patterning occurs voxel by voxel. However, DLP printing requires the ability to control layer thickness (e.g. by controlling light attenuation) with the final structural dimension in mind. Here, we optimized the layer thickness for 10 μm features, which maximize printing speed while maintaining the cellular scale resolution needed for patterning crypt-like overhang structures found in intestinal organoids. To fabricate structures at other length scales ranging from subcellular to macroscopic, further optimization of the layer thickness and cure depth could be readily performed.

Lastly, we showed that Matrigel features patterned with this method support the growth of ISC monolayers, and successfully imparts geometry to the epithelial layer which conforms to the designed pattern. Recent advances to primary-cell derived monolayer culture platforms have focused on the optimization of culture and substrate conditions in attempt to replicate *in vivo* intestinal function [48–50]. However, these *in vitro* monolayer cultures have not considered the shape of the crypt-villus axis, which imparts three-dimensional behavior onto the intestinal epithelium and is necessary to generate morphogen gradients [51] and cell shape changes [52, 53] essential for proper development. While there has been some work to incorporate 3D topologies into intestinal monolayer cultures, these applications have relied on the use of PDMS or 3D printed plastic stamps to generate topology [10, 54]. As a soft lithographic technique, stamping to create patterned features for intestinal monolayers has only been used to create simple features in stiff hydrogels ($G' > 8$ kPa) [10, 54]. In effect, this limits the cell morphologies and behaviors that are attainable. For example, substrate stiffness has been shown to influence crypt domain morphology in 2D monolayers [55] and 3D encapsulated organoids [3, 56]. With PDMS stamps, monolayer cultures are restricted to stiff materials, thus limiting the range of biological behaviors that are attainable. Instead, we show that printed thioester features can be transferred into a variety of soft, biologically relevant materials (<1000 Pa), while still maintaining feature resolution. This platform enables the ability to more thoroughly investigate specific intestinal disease states, like fibrosis, in which substrate stiffness is a contributing factor [57]. Additionally, our platform enables the generation of complex, overhanging features that cannot be realized with PDMS stamping. The shape of the crypt-villus axis is known to direct cell fate specification in the developing intestine [52, 58] and the ability to create complex and physiologically relevant 3D shapes with greater resolution will offer greater insight into these developmental processes.

5. Conclusion

Intestinal organoids have become important tools for studying fundamental biology and modeling disease *in vitro*. With control over geometry and shape becoming increasingly important in some complex intestinal organoid systems, we sought to develop a new biofabrication approach that could match resolution of soft lithographic approaches while maintaining advantages of 3D printing, like forming high resolution overhanging features. In this work, we present a novel elastomer resin that is compatible with state of the art light based 3D printing techniques and undergoes rapid degradation in the presence of 2-mercaptoethanol. We show that thioester elastomer resin can be printed using DLP 3D printing at resolution and feature sizes at and above 30 μm. The subsequent feature erosion was triggered by the introduction of a thiol to solution and was gentile enough to be used in the presence of Matrigel. This work shines a light on the potential of sacrificial resins based on covalent adaptable chemistries by introducing a novel fabrication method for organoid structures with complex geometries. This tool expands on existing biofabrication methods and allows for the testing of new hypotheses related to the role geometry plays in complex organoid cultures.

Data availability statement

The data that support the findings of this study are available upon reasonable request from the authors.

Acknowledgments

This work was supported by grants from the National Institutes of Health (DE016523, R01 DK120921), and the National Science Foundation (1826454). J J H recognizes support from the Department of Education program 'Graduate Assistantships in Areas of National Need' (GAANN). F M Y acknowledges the Department of Education (GAANN) and the National Institutes of Health (F31 DK126427) for funding. Image and data analysis were assisted by Jian Wei Tay, PhD, at the BioFrontiers Institute Advanced Light Microscopy Core (RRID: SCR_018302). The authors would also like to thank Dr Laura Macdougall, Dr Michael Blatchley, Dr Benjamin Richardson, and Dr Kemal Arda Günay for thoughtful comments and critical reviews in the preparation of this manuscript. The authors do not have any conflicts of interest to declare.

ORCID iDs

Juan J Hernandez https://orcid.org/0000-0003-0040-0904
Kristi S Anseth https://orcid.org/0000-0002-5725-5691

References

[1] Hofer M and Lutolf M P 2021 Engineering organoids *Nat. Rev. Mater.* **6** 402–20
[2] Sato T and Clevers H 2013 Growing self-organizing mini-guts from a single intestinal stem cell: mechanism and applications *Science* **340** 1190–4
[3] Hushka E A, Yavitt F M, Brown T E, Dempsey P J and Anseth K S 2020 Relaxation of extracellular matrix forces directs crypt formation and architecture in intestinal organoids *Adv. Healthcare Mater.* **9** 1901214
[4] Lancaster M A and Knoblich J A 2014 Organogenesis in a dish: modeling development and disease using organoid technologies *Science* **345** 1247125
[5] Nerger B A and Nelson C M 2019 3D culture models for studying branching morphogenesis in the mammary gland and mammalian lung *Biomaterials* **198** 135–45
[6] Gjorevski N *et al* 2016 Designer matrices for intestinal stem cell and organoid culture *Nat. Publ. Gr.* **539** 560–64
[7] Gjorevski N *et al* Tisse geometry drives deterministic organoid patterning *Unpublished*
[8] Tan E Y S, Suntornnond R and Yeong W Y 2021 High-resolution novel indirect bioprinting of low-viscosity cell-laden hydrogels via model-support bioink interaction *3D Print. Addit. Manuf.* **8** 69–78
[9] Ma X *et al* 2016 Deterministically patterned biomimetic human iPSC-derived hepatic model via rapid 3D bioprinting *Proc. Natl Acad. Sci. USA* **113** 2206–11
[10] Wang Y *et al* 2017 A microengineered collagen scaffold for generating a polarized crypt-villus architecture of human small intestinal epithelium *Biomaterials* **128** 44–55
[11] Datta P, Ayan B and Ozbolat I T 2017 Bioprinting for vascular and vascularized tissue biofabrication *Acta Biomater.* **51** 1–20
[12] Golden A P and Tien J 2007 Fabrication of microfluidic hydrogels using molded gelatin as a sacrificial element *Lab Chip* **7** 720
[13] Miller J S *et al* 2012 Rapid casting of patterned vascular networks for perfusable engineered three-dimensional tissues *Nat. Mater.* **11** 768–74
[14] Kolesky D B *et al* 2014 3D bioprinting of vascularized, heterogeneous cell-laden tissue constructs *Adv. Mater.* **26** 3124–30
[15] Kolesky D B, Homan K A, Skylar-Scott M A and Lewis J A 2016 Three-dimensional bioprinting of thick vascularized tissues *Proc. Natl Acad. Sci. USA* **113** 3179–84
[16] Pasturel A, Strale P O and Studer V 2020 Tailoring common hydrogels into 3D cell culture templates *Adv. Healthcare Mater.* **9** 2000519
[17] Nikolaev M *et al* 2020 Homeostatic mini-intestines through scaffold-guided organoid morphogenesis *Nature* **585** 574–8
[18] Arakawa C *et al* 2020 Biophysical and biomolecular interactions of malaria-infected erythrocytes in engineered human capillaries *Sci. Adv.* **6** eaay7243
[19] Brandenberg N and Lutolf M P 2016 *In situ* patterning of microfluidic networks in 3D cell-laden hydrogels *Adv. Mater.* **28** 7450–6
[20] Guzzi E A and Tibbitt M W 2019 Additive manufacturing of precision biomaterials *Adv. Mater.* **32** 1901994
[21] Kinstlinger I S *et al* 2020 Generation of model tissues with dendritic vascular networks via sacrificial laser-sintered carbohydrate templates *Nat. Biomed. Eng.* **4** 916–32
[22] Thomas A *et al* 2020 Vascular bioprinting with enzymatically degradable bioinks via multi-material projection-based stereolithography *Acta Biomater.* **117** 121–32
[23] Schultz K M and Anseth K S 2013 Monitoring degradation of matrix metalloproteinases-cleavable PEG hydrogels via multiple particle tracking microrheology *Soft Matter* **9** 1570–9
[24] Rice M A, Sanchez-Adams J and Anseth K S 2006 Exogenously triggered, enzymatic degradation of photopolymerized hydrogels with polycaprolactone subunits: experimental observation and modeling of mass loss behavior *Biomacromolecules* **7** 1968–75
[25] Brown T E *et al* 2018 Photopolymerized dynamic hydrogels with tunable viscoelastic properties through thioester exchange *Biomaterials* **178** 496–503
[26] Worrell B T *et al* 2018 Bistable and photoswitchable states of matter *Nat. Commun.* **9** 2804
[27] Carberry B J, Rao V V and Anseth K S 2020 Phototunable viscoelasticity in hydrogels through thioester exchange *Ann. Biomed. Eng.* **48** 2053–63
[28] Ghobril C, Charoen K, Rodriguez E K, Nazarian A, Grinstaff M W and Dendritic Thioester A 2013 Hydrogel based on thiol-thioester exchange as a dissolvable sealant system for wound closure *Angew. Chem., Int. Ed.* **52** 14070–4
[29] Konieczynska M D *et al* 2016 On-demand dissolution of a dendritic hydrogel-based dressing for second-degree burn wounds via thiol-thioester exchange reaction HHS public access *Angew. Chem., Int. Ed. Engl.* **55** 9984–7
[30] Macdougall L J, Pérez-Madrigal M M, Arno M C and Dove A P 2018 Nonswelling thiol-yne cross-linked hydrogel materials as cytocompatible soft tissue scaffolds *Biomacromolecules* **19** 1378–88
[31] Miller D B, Alim M D and McLeod R R 2019 Reflection suppression via elastomeric films *Opt. Lett.* **44** 6021
[32] Urness A C, Moore E D, Kamysiak K K, Cole M C and McLeod R R 2013 Liquid deposition photolithography for submicrometer resolution three-dimensional index structuring with large throughput *Light Sci. Appl.* **2** e56
[33] Dendukuri D *et al* 2008 Modeling of oxygen-inhibited free radical photopolymerization in a PDMS microfluidic device *Macromolecules* **41** 8547–56
[34] Nelson C M, van Duijn M M, Inman J L, Fletcher D A and Bissell M J 2006 Tissue geometry determines sites of mammary branching morphogenesis in organotypic cultures *Science* **314** 298–300
[35] Nelson C M, Inman J L and Bissell M J 2008 Three-dimensional lithographically defined organotypic

tissue arrays for quantitative analysis of morphogenesis and neoplastic progression *Nat. Protocols* **3** 674–8
[36] Fairbanks B D *et al* 2009 A versatile synthetic extracellular matrix mimic via thiol-norbornene photopolymerization *Adv. Mater.* **21** 5005–10
[37] Worrell B T *et al* 2018 A user's guide to the thiol-thioester exchange in organic media: scope, limitations, and applications in material science *Polym. Chem.* **9** 4523–34
[38] Kamata H, Akagi Y, Kayasuga-Kariya Y, Chung U I and Sakai T 2014 Nonswellable' hydrogel without mechanical hysteresis *Science* **343** 873–5
[39] Kamata H, Kushiro K, Takai M, Chung U and Sakai T 2016 Non-osmotic hydrogels: a rational strategy for safely degradable hydrogels *Angew. Chem., Int. Ed.* **55** 9282–6
[40] Muralidharan A, Uzcategui A C, McLeod R R and Bryant S J 2019 Stereolithographic 3D printing for deterministic control over integration in dual-material composites *Adv. Mater. Technol.* **4** 1900592
[41] Higgins C I, Brown T E and Killgore J P 2021 Digital light processing in a hybrid atomic force microscope: *in situ*, nanoscale characterization of the printing process *Addit. Manuf.* **38** 101744
[42] Rubinstein M and Colby R H 2003 *Polymer Physics* (Oxford: Oxford University Press)
[43] Hiemenz P C and Lodge T P 2007 *Polymer Chemistry* 2nd edn (Boca Raton, FL: CRC Press)
[44] Chaudhuri O, Cooper-White J, Janmey P A, Mooney D J and Shenoy V B 2020 Effects of extracellular matrix viscoelasticity on cellular behaviour *Nature* **584** 535–46
[45] Chaudhuri O *et al* 2015 Substrate stress relaxation regulates cell spreading *Nat. Commun.* **6** 6365
[46] Fu Y Y *et al* 2009 Microtome-free 3-dimensional confocal imaging method for visualization of mouse intestine with subcellular-level resolution *Gastroenterology* **137** 453–65
[47] Brassard J A and Lutolf M P 2019 Cell stem cell review engineering stem cell self-organization to build better organoids *Stem Cell* **24** 860–76
[48] Tong Z *et al* 2018 Towards a defined ECM and small molecule based monolayer culture system for the expansion of mouse and human intestinal stem cells *Biomaterials* **154** 60–73
[49] Moon C, Vandussen K L, Miyoshi H and Stappenbeck T S 2013 Development of a primary mouse intestinal epithelial cell monolayer culture system to evaluate factors that modulate IgA transcytosis *Mucosal Immunol.* **7** 818–28
[50] Liu Y, Qi Z, Li X, Du Y and Chen Y G 2018 Monolayer culture of intestinal epithelium sustains Lgr5+ intestinal stem cells *Cell Discovery* **4** 4–6
[51] Shyer A E, Huycke T R, Lee C, Mahadevan L and Tabin C J 2015 Bending gradients: how the intestinal stem cell gets its home *Cell* **161** 569–80
[52] Sumigray K D, Terwilliger M and Lechler T 2018 Morphogenesis and compartmentalization of the intestinal crypt *Dev. Cell* **45** 183–197.e5
[53] Luciano M *et al* 2020 Large-scale curvature sensing by epithelial monolayers depends on active cell mechanics and nuclear mechanoadaptation (*bioRxiv*)
[54] Wilson R L *et al* 2020 Protein-functionalized poly(ethylene glycol) hydrogels as scaffolds for monolayer organoid culture *Tissue Eng.* C **27** 12–23
[55] Pérez-González C *et al* 2020 Mechanical compartmentalization of the intestinal organoid enables crypt folding and collective cell migration (*bioRxiv*) pp 1–26
[56] Yavitt F M *et al* 2020 The effect of thiol structure on allyl sulfide photodegradable hydrogels and their application as a degradable scaffold for organoid passaging *Adv. Mater.* **32** 1905366
[57] Johnson L A *et al* 2013 Matrix stiffness corresponding to strictured bowel induces a fibrogenic response in human colonic fibroblasts *Inflamm. Bowel Dis.* **19** 891–903
[58] Walton K D, Mishkind D, Riddle M R, Tabin C J and Gumucio D L 2018 Blueprint for an intestinal villus: species-specific assembly required *Wiley Interdiscip. Rev. Dev. Biol.* **7** 1–19